# Unresolved sideband photon recoil spectroscopy of molecular ions

E. H. Clausen, V. Jarlaud, K. Fisher, S. Meyer, C. Solaro, and M. Drewsen

Department of Physics and Astronomy, Aarhus University, DK-8000 Aarhus C, Denmark

**ARTICLE HISTORY**
Compiled April 8, 2020

**ABSTRACT**
We reflect on the prospect of exploiting the recoil associated with absorption and emission of photons to perform spectroscopy of a single molecular ion. For this recoil to be detectable, the molecular ion is sympathetically cooled by a laser-cooled atomic ion to near the quantum mechanical ground state of a common trapping potential. More specifically, we present a general framework for simulating the expected photon recoil spectra in regimes where either the natural transition linewidth $\Gamma_t$ of the molecular ion or the spectral width $\Gamma_L$ of the exciting light source exceeds the motional angular frequencies (typically $\sim 2\pi \times 0.1 - 1$ MHz) of the two-ion system. To exemplify the framework, we present two complementary cases: spectroscopy of the broad 3s $^2S_{1/2}$ - 3p $^2P_{3/2}$ electronic transition ($\Gamma_t/2\pi = 41.8$ MHz) of a single $^{24}Mg^+$ ion at $\lambda = 279.6$ nm by a narrow laser source ($\Gamma_L/2\pi \lesssim 1$ MHz) and mid-infrared vibrational spectroscopy of the very narrow $|v = 0, J = 1\rangle$ - $|v' = 1, J' = 0\rangle$ transition ($\Gamma_t/2\pi = 2.50$ Hz) at $\lambda = 6.17\,\mu$m in the $^1\Sigma^+$ electronic ground state of $^{24}MgH^+$ by a broadband laser source ($\Gamma_L/2\pi \gtrsim 10$ MHz). The atomic ion $^{24}Mg^+$ has been picked to introduce a simple system to make comparisons with experimental results while still capturing most of the physics involved in electronic excitations of molecular ions.

**KEYWORDS**
Single molecule spectroscopy; photon recoil; sympathetic cooling; molecular ion trapping

## 1. Introduction

In the past two decades, it has become possible to trap and sympathetically cool ensembles of molecular ions in the gas phase to the millikelvin range, where they become part of so-called Coulomb crystals through interactions with simultaneously trapped and laser-cooled atomic ions [1]. More recently, single molecular ions have even been sympathetically cooled to microkelvin-temperatures by single atomic ions where the common modes of the strongly coupled two-ion system are close to their quantum mechanical ground states [2–4]. The latter scenario constitutes a novel setting for conducting molecular spectroscopy with potentially very high resolution for fundamental structure-studies of molecular ions, test of fundamental physics theories and quantum technology oriented applications [5–9]. However, since it is practically impossible to count a single absorbed photon from a light beam, or to detect with high probability a single photon emitted by a single molecular ion, standard absorption and emission

CONTACT C. Solaro. Email: solaro@phys.au.dk
CONTACT M. Drewsen. Email: drewsen@phys.au.dk

spectroscopy cannot be applied efficiently. The solution to this problem is photon recoil spectroscopy (PRS) [10–12], where it is the momentum recoil associated with absorption and emission of individual photons by a single target ion that signalizes a spectroscopic event through the excitation of the common motion of the two-ion system. Since PRS has been already applied to ultra-precise spectroscopy of atomic ions [13] and should be largely applicable to molecular ions as well, it holds great promises for ultra-high resolution spectroscopy of molecular ions in the near future [9]. Besides, PRS is also interesting for a range of other investigations of molecules in the gas phase. Specific implementations of this technique could include internal state preparation of molecules, e.g. for state to state reaction experiments, or single photon absorption studies of single, complex, molecular ions under well-controlled conditions. In the latter example, the technique can even be applied in situations where the absorption leads to complete internal energy conversion.

In the following section (Sec. 2), we will discuss in detail the basics of photon recoil spectroscopy and present a mathematical framework which can be used to simulate photon recoil spectra in the special cases where the spectra are unresolved with respect to the motional sidebands, either due to naturally occurring broad spectroscopic transitions of linewidth $\Gamma_t$ or due to the linewidth $\Gamma_L$ of the applied light sources. This generic section will serve as the basis for the next section (Sec. 3), where we present simulated results for the spectroscopy of the broad 3s $^2S_{1/2}$ - 3p $^2P_{3/2}$ electronic transition ($\Gamma_t/2\pi = 41.8\,\mathrm{MHz}$ [14, 15]) of a single $^{24}Mg^+$ ion at $\lambda = 279.6$ nm by a narrow laser source ($\Gamma_L/2\pi \lesssim 1$ MHz), and mid-infrared vibrational spectroscopy by a broadband laser source ($\Gamma_L/2\pi \gtrsim 10$ MHz) of the very narrow $|v = 0, J = 1\rangle$ - $|v' = 1, J' = 0\rangle$ transition ($\Gamma_t/2\pi = 2.50$ Hz [16, 17]) at $\lambda = 6.17\,\mu\mathrm{m}$ in the $^1\Sigma^+$ electronic ground state of $^{24}MgH^+$. The prospects and limitations of unresolved PRS are discussed in Sec. 4 before the conclusion in Sec. 5.

## 2. Model for unresolved sideband photon recoil spectroscopy

The idea of exploiting the photon recoil associated with absorption and emission in connection with spectroscopy was first devised by the Nobel laureate Prof. Wineland. It was done with the prospect of developing optical atomic clocks based on single atomic ions with suitable narrow optical transitions, but lacking transitions for direct laser cooling [10, 18]. In this case, the spectroscopy is carried out by trapping a single spectroscopic target ion together with a single atomic ion that can be sideband cooled. Through the Coulomb interaction between the ions, the two-ion system can be brought to the quantum mechanical ground state with respect to one or more motional modes. In the original paper, the authors consider a so-called resolved sideband scenario where the two motional mode angular frequencies corresponding to the in-phase mode ($\omega_{ip}$) and out-of-phase mode ($\omega_{op}$) are significantly larger than both the transition linewidth and the spectral width of the spectroscopy laser. In this scenario, it is possible to selectively address both the spectroscopy ion (target ion) and the sideband-cooling ion (readout ion) with lasers tuned resonantly to either carrier or specific motional sideband transitions. Fig. 1 illustrates one of the simplest specific implementations of PRS capturing the elements important to the present paper. This procedure starts by (i) initializing the two-ion system in the quantum mechanical ground state of at least one of the two motional modes along the axis defined by the two ions (e.g. the out-of-phase mode), the readout atomic ion in its electronic ground state, and the molecular ion in its internal target state for the spectroscopy. Next, the target molecular ion is

exposed to a light pulse expected to be resonant with the blue sideband (BSB) of the spectroscopy transition (i.e. $\omega_L = \omega_t + \omega_{op}$, where $\omega_L$, $\omega_t$ are the angular frequencies of the light and of the target transition respectively). If the correct interaction time $\tau_{spec}$ is chosen, the resonant BSB pulse leads to a full excitation of the target ion to $|e_t\rangle$ (see the more complete theoretical description below), and the two-ion system is transferred to the state depicted in (ii) where the out-of-phase mode is now in its first excited state ($n_{op} = 1$). This motional excitation can be monitored by addressing the readout atomic ion with a light pulse resonant with the red sideband (RSB) of the narrow sideband cooling transition ($\omega_L = \omega_r - \omega_{op}$, where $\omega_r$ is the transition frequency) for a time $\tau_r$ corresponding to a full excitation to the $|e_r\rangle$ state at the expense of the motional excitation (iii). In the final step (iv), the readout ion is exposed to light resonant with a closed fast fluorescing transition $|g_r\rangle$ - $|f_r\rangle$. This leads to the emission of a large amount of photons at the frequency $\omega_f$ if the readout ion was in the $|g_r\rangle$ state against no photon emission if in the $|e_r\rangle$ state. Since we assumed in step (iii) to have brought the readout ion to the $|e_r\rangle$ state, we expect no fluorescence in the last step (iv) if the pulse applied to the target molecular ion was indeed excited by the first BSB pulse. Conversely, if the target ion was not excited on the BSB, the readout ion would stay in the $|g_r\rangle$ state after step (iii), and fluorescence light would be emitted during the final step (iv). Hence, through repetition of the sequence (i)-(iv) for different values of $\omega_L$ when addressing the target ion, the total fluorescence signal from the readout atomic ion will reflect the excitation probability of the target molecular ion and thus produce a spectroscopy signal. Based on a mathematical framework which can be applied to simulate the expected spectroscopy signal for the resolved sideband scenario above, we will establish in the end of this section a general framework to also describe the expected signal for the situation depicted in Fig. 1 in unresolved sideband regimes.

### *2.1. Hamiltonian dynamics relevant to PRS in the resolved sideband regime*

In the following we consider the situation presented in Fig. 1 with the two ions, the target and the readout ion, both confined in a trap along the $z$-axis (e.g. the rf free axis of a linear rf trap) thanks to suitable high trapping frequencies in the perpendicular plane. We assume that the internal states of the two ions are the same as the ones defined in Fig. 1. The target ion has a simple two-level structure $\{|g_t\rangle, |e_t\rangle\}$ which leads to the internal state Hamiltonian

$$\hat{H}_t = \frac{\hbar\omega_t}{2}\left(|e_t\rangle\langle e_t| - |g_t\rangle\langle g_t|\right) \tag{1}$$

with $\hbar\omega_t = E_{e,t} - E_{g,t}$, where $E_{g,t}$ and $E_{e,t}$ are the energies of the two states. The readout ion has the three-level structure $\{|g_r\rangle, |e_r\rangle, |f_r\rangle\}$. It reduces to the two levels $|g_r\rangle$ and $|e_r\rangle$ when considering only the Hamiltonian evolution of the PRS scheme before readout (steps i) to iii), Fig. 1). The internal state Hamiltonian is thus

$$\hat{H}_r = \frac{\hbar\omega_r}{2}\left(|e_r\rangle\langle e_r| - |g_r\rangle\langle g_r|\right) \tag{2}$$

with $\hbar\omega_r = E_{e,r} - E_{g,r}$, where $E_{g,r}$ and $E_{e,r}$ are the energies of the two states. In addition to the two ions' internal states, the external motional states of the two-ion

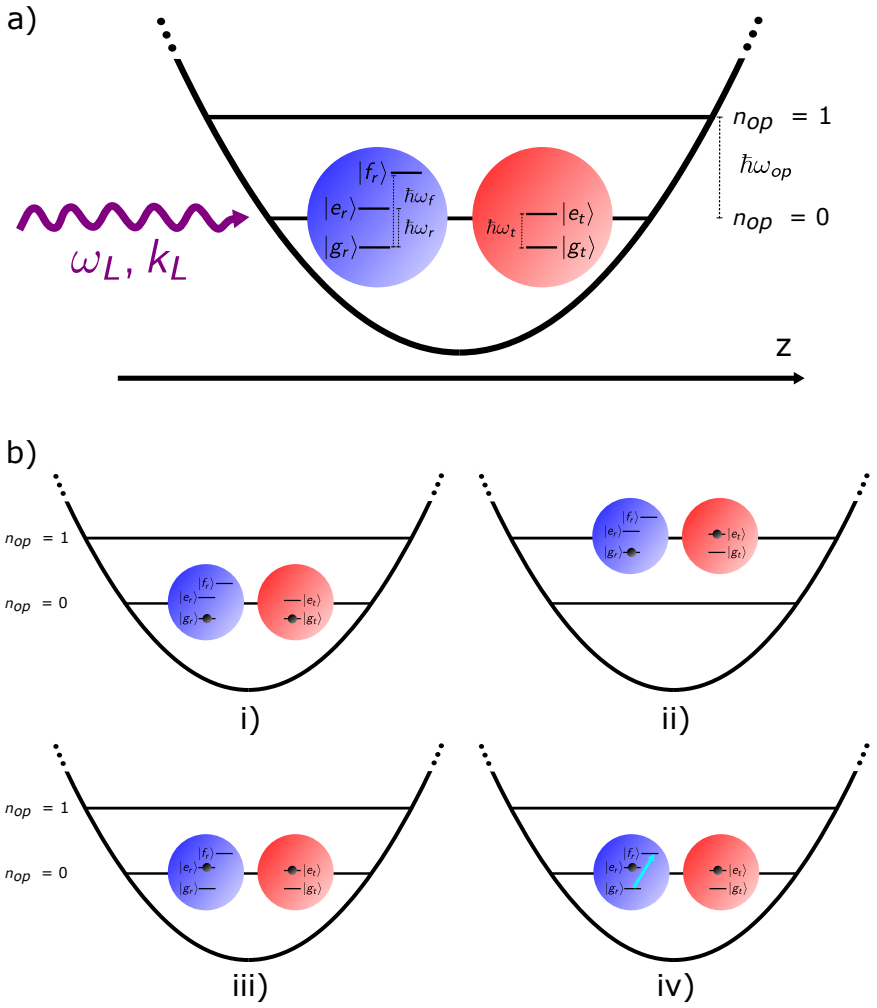


**Figure 1.** a) A single spectroscopic target ion (red) is trapped together with one readout atomic ion (blue) in a linear Paul trap. Doppler cooling followed by sideband cooling on the readout ion ensures that the two-ion Coulomb crystal sits in the motional ground state along the z-direction. The simplified internal structure of each ion is also shown: the target ion has a simple two-level structure and the readout ion has a three-level structure made of two narrow states and one short-lived state used for fluorescence detection. A light field of frequency $\omega_L$ propagating along z interacts with one of the two ions only.
b) Schematic of photon recoil spectroscopy. i) The two-ion system is initialized in its motional ground state with respect to e.g. the out-of-phase mode of motion. The readout ion is prepared in its electronic ground state and the molecular ion in its internal target state. ii) After a resonant blue-sideband spectroscopy pulse on the target ion, the two-ion system is transferred to the first excited state $n_{op} = 1$. iii) After a resonant red-sideband pulse on the readout ion, the two-ion system is transferred back to the motional ground state, the readout ion is in the $|e_r\rangle$ state. iv) When exposed to light resonant with the $|g_r\rangle \leftrightarrow |f_r\rangle$ transition, the readout ion does not fluoresce, reflecting a successful excitation of the target ion by the blue-sideband pulse before step ii).

system along the $z$-axis can be described by the following Hamiltonian

$$\hat{H}_z = \hbar\omega_{ip}\left(\hat{a}_{ip}^{\dagger}\hat{a}_{ip} + \frac{1}{2}\right) + \hbar\omega_{op}\left(\hat{a}_{op}^{\dagger}\hat{a}_{op} + \frac{1}{2}\right) \tag{3}$$

where we have introduced the standard harmonic oscillator ladder operators $\hat{a}_{ip}^{\dagger}$, $\hat{a}_{ip}$ and $\hat{a}_{op}^{\dagger}$, $\hat{a}_{op}$ for the in-phase (IP) and out-of-phase (OP) modes respectively. The associated mode angular frequencies, for singly charged ions, are given by [19, 20]:

$$\begin{aligned}\omega_{ip} &= \omega_z\left(1 + \frac{1}{\mu} - \sqrt{1 - \frac{1}{\mu} + \frac{1}{\mu^2}}\right)^{1/2} \\ \omega_{op} &= \omega_z\left(1 + \frac{1}{\mu} + \sqrt{1 - \frac{1}{\mu} + \frac{1}{\mu^2}}\right)^{1/2}\end{aligned} \tag{4}$$

with $\mu = m_t/m_r$ being the ion mass ratio and $\omega_z$ the motional angular frequency of the readout ion if it were alone in the trap, all trapping parameters being the same. Essential for PRS is the Hamiltonian describing the light induced interaction between the internal and external degrees of freedom of the ions. We assume here that the light field can be approximated by a monochromatic plane wave with angular frequency $\omega_L$ travelling along the $z$-axis. Furthermore, we assume that the difference between the two transition angular frequencies $\omega_t$ and $\omega_r$ is large enough so that a light field close to resonance with one of the ions will not perturb the other. In this case, one can write up the Hamiltonian for the light interaction as

$$\hat{H}_{int,j} = \hbar\Omega_{0,j}\cos(k_L\hat{z}_j - \omega_L t)(|e_j\rangle\langle g_j| + |g_j\rangle\langle e_j|) \quad , \quad j \in \{r, t\} \tag{5}$$

with $\Omega_{0,j}$ the vacuum Rabi angular frequency associated with the particular light field and oscillator strength and $\vec{k}_L$ the wave vector of the laser field.
The coupling of the ions' internal and external degrees of freedom appears through the position operator $\hat{z}_j$ of the interaction Hamiltonian. This operator can be written for both ions in terms of the ladder operators as [21–23]

$$\hat{z}_j = |b_{ip,j}|\sqrt{\frac{\hbar}{2m_j\omega_{ip}}}(\hat{a}_{ip}^{\dagger} + \hat{a}_{ip}) + |b_{op,j}|\sqrt{\frac{\hbar}{2m_j\omega_{op}}}(\hat{a}_{op}^{\dagger} + \hat{a}_{op}) \tag{6}$$

where $b_{ip,j}$ and $b_{op,j}$ are the components of the eigenvectors (in a mass-weighted space) for the IP and OP modes respectively. They can be written for the readout and target ions as

$$\begin{aligned}b_{ip/op,r} &= \frac{r_{ip/op}}{\sqrt{1 + r_{ip/op}^2}} \\ b_{ip/op,t} &= \frac{1}{\sqrt{1 + r_{ip/op}^2}}\end{aligned} \tag{7}$$

with

$$
\begin{aligned}
r_{ip} &= \frac{-\mu + 1 + \sqrt{\mu^2 - \mu + 1}}{\sqrt{\mu}} \\
r_{op} &= \frac{-\mu + 1 - \sqrt{\mu^2 - \mu + 1}}{\sqrt{\mu}}.
\end{aligned}
\tag{8}
$$

Introducing the Lamb-Dicke parameters (LDP) [19]

$$
\begin{aligned}
\eta_{ip,j} &= \vec{k}_L \cdot \hat{z} |b_{ip,j}| \sqrt{\frac{\hbar}{2 m_j \omega_{ip}}} \\
\eta_{op,j} &= \vec{k}_L \cdot \hat{z} |b_{op,j}| \sqrt{\frac{\hbar}{2 m_j \omega_{op}}}
\end{aligned}
\tag{9}
$$

we can rewrite the interaction Hamiltonian as

$$
\hat{H}_{int,j} = \hbar \Omega_{0,j} \cos\left(\eta_{ip,j}(\hat{a}_{ip}^\dagger + \hat{a}_{ip}) + \eta_{op,j}(\hat{a}_{op}^\dagger + \hat{a}_{op}) - \omega_L t\right)\left( |e_j\rangle \langle g_j| + |g_j\rangle |e_j\rangle \right).
\tag{10}
$$

The full Hamiltonian is given by

$$
\hat{H}_{tot} = \hat{H}_r + \hat{H}_t + \hat{H}_z + \hat{H}_{int,j} \equiv \hat{H}_0 + \hat{H}_{int,j}.
\tag{11}
$$

In order to investigate the dynamics of the interaction between the internal and external degrees of freedom, it is convenient to work in the interaction picture through the transformation

$$
\hat{H}_I = e^{i\hat{H}_0 t/\hbar} \hat{H}_{int,j} e^{-i\hat{H}_0 t/\hbar}
\tag{12}
$$

which, due to the commutativity between the internal and external state operators, leads to

$$
\begin{aligned}
\hat{H}_I = &\hbar \Omega_{0,j} \Big( e^{i\omega_j t} |e_j\rangle \langle g_j| + e^{-i\omega_j t} |g_j\rangle \langle e_j| \Big) \times \\
&e^{i\hat{H}_z t/\hbar} \cos\left(\eta_{ip,j}(\hat{a}_{ip}^\dagger + \hat{a}_{ip}) + \eta_{op,j}(\hat{a}_{op}^\dagger + \hat{a}_{op}) - \omega_L t\right) e^{-i\hat{H}_z t/\hbar}.
\end{aligned}
\tag{13}
$$

Performing the rotating wave approximation, i.e. keeping time dependent terms containing $\omega_j - \omega_L$ and not the ones containing $\omega_j + \omega_L$, one arrives at:

$$
\hat{H}_I = \frac{\hbar}{2} \Omega_{0,j} |e_j\rangle \langle g_j| e^{i\hat{H}_z t/\hbar} e^{i(\eta_{ip,j}(\hat{a}_{ip} + \hat{a}_{ip}^\dagger) + \eta_{op,j}(\hat{a}_{op} + \hat{a}_{op}^\dagger) - \delta_j t)} e^{-i\hat{H}_z t/\hbar} + h.c.,
\tag{14}
$$

where we have introduced the laser detuning $\delta_j = \omega_L - \omega_j$. By introducing the time scaled ladder operators

$$
\begin{aligned}
\tilde{\hat{a}}_{ip} = \hat{a}_{ip} e^{-i\omega_{ip} t} \quad &, \quad \tilde{\hat{a}}_{ip}^\dagger = \hat{a}_{ip}^\dagger e^{i\omega_{ip} t} \\
\tilde{\hat{a}}_{op} = \hat{a}_{op} e^{-i\omega_{op} t} \quad &, \quad \tilde{\hat{a}}_{op}^\dagger = \hat{a}_{op}^\dagger e^{i\omega_{op} t}
\end{aligned}
\tag{15}
$$

and using the Baker-Campbell-Haussdor formula for decomposing the exponential term [24], one can re-express the interaction Hamiltonian as

$$\hat{H}_I = \frac{\tilde{\ }_{0_j}}{2} |e_j\rangle\langle g_j| e^{i\ _j t} e^{\ ^2_{ip;j}=2} e^{\ ^2_{op;j}=2} e^{i\ _{ip;j}\hat{a}^\dagger_{ip}} e^{i\ _{ip;j}\hat{a}_{ip}} e^{i\ _{op;j}\hat{a}^\dagger_{op}} e^{i\ _{op;j}\hat{a}_{op}} + h.c. \quad (16)$$

The specific quantum dynamics now depends on which ion we address with the light field. Next, one has to solve the Schrödinger equation of motion

$$i\tilde{\ }\frac{\partial}{\partial t}|\ (t)\rangle = \hat{H}|\ (t)\rangle \quad (17)$$

in the state-basis of $|i_r; i_t; n_{ip}; n_{op}\rangle$, where $|i_j\rangle$ indicates the internal state $i \in \{g; e\}$ of the ion $j \in \{r; t\}$. In the case where the readout ion is addressed by the light field, we obtain the following interaction matrix elements [25]:

$$\langle e_r; i_t; n'_{ip}; n'_{op}|\hat{H}_I|g_r; i_t; n_{ip}; n_{op}\rangle = \frac{\tilde{\ }_{0;r}}{2} e^{i(s_{ip}\ _{ip} + s_{op}\ _{op}\ \ _r)t} e^{\ ^2_{ip;r}=2} e^{\ ^2_{op;r}=2} \sum_{m_{ip}=0}^{n^<_{ip}} \sum_{m_{op}=0}^{n^<_{op}} \frac{(i\ _{ip;r})^{2m_{ip}+|s_{ip}|}\sqrt{n^<_{ip}!n^>_{ip}!}}{m_{ip}!(m_{ip}+|s_{ip}|)!(n^<_{ip}-m_{ip})!} \frac{(i\ _{op;r})^{2m_{op}+|s_{op}|}\sqrt{n^<_{op}!n^>_{op}!}}{m_{op}!(m_{op}+|s_{op}|)!(n^<_{op}-m_{op})!} \quad (18)$$

where $s_{ip=op} = n'_{ip=op} - n_{ip=op}$ is the sideband order, $n^<_{ip=op} = \min\{n_{ip=op}; n'_{ip=op}\}$ and $n^>_{ip=op} = \max\{n_{ip=op}; n'_{ip=op}\}$. In a slightly more compact form, we can rewrite this expression as:

$$\langle e_r; i_t; n'_{ip}; n'_{op}|\hat{H}_I|g_r; i_t; n_{ip}; n_{op}\rangle = \frac{\tilde{\ }_{0;r}}{2} e^{i(s_{ip}\ _{ip} + s_{op}\ _{op}\ \ _r)t} \quad (\ _{ip};\ _{op}; n_{ip}; n_{op}; s_{ip}; s_{op}) \quad (19)$$

with

$$(\ _{ip};\ _{op}; n_{ip}; n_{op}; s_{ip}; s_{op}) = e^{\ ^2_{ip;r}=2}(i\ _{ip;r})^{|s_{ip}|}\sqrt{\frac{n^<_{ip}}{n^>_{ip}}}L^{|s_{ip}|}_{n^<_{ip}}(\ ^2_{ip;r}) \; e^{\ ^2_{op;r}=2}(i\ _{op;r})^{|s_{op}|}\sqrt{\frac{n^<_{op}}{n^>_{op}}}L^{|s_{op}|}_{n^<_{op}}(\ ^2_{op;r}) \quad (20)$$

where $L^{|s_{ip}|}_{n^<_{ip}}(\ ^2_{ip;r})$ and $L^{|s_{op}|}_{n^<_{op}}(\ ^2_{op;r})$ are the generalized Laguerre polynomials. One can see from eq. (19) that, for the monochromatic situation considered now, dynamics involving transitions with specific changes in motional quantum numbers can be efficient by tuning the laser field to be resonant with a specific sideband, i.e.,

$$s_{ip}\ _{ip} + s_{op}\ _{op}\ \ _r = 0: \quad (21)$$

In this case the explicit time dependence in the coupling matrix elements vanishes for the particular type of transitions, while the off-resonant coupling terms to other transitions will generally average to zero. The Rabi angular frequency for a specific

sideband and motional state is thus given by [21]:

$$\Omega_{n_{ip},n_{op},s_{ip},s_{op}} = \Omega_{0,r}\xi(\eta_{ip},\eta_{op},n_{ip},n_{op},s_{ip},s_{op}). \tag{22}$$

The situation becomes particularly simple in the so-called Lamb-Dicke regime where $\eta_{ip/op}\sqrt{2\langle n_{ip/op}\rangle + 1} \ll 1$. In this case, we can simplify Eq. (20) to [21]:

$$\xi(\eta_{ip},\eta_{op},n_{ip},n_{op},s_{ip},s_{op}) = \left(\frac{\eta_{ip,r}^{|s_{ip}|}}{|s_{ip}|!}\sqrt{\frac{n_{ip}^{>}!}{n_{ip}^{<}!}}\right)\left(\frac{\eta_{op,r}^{|s_{op}|}}{|s_{op}|!}\sqrt{\frac{n_{op}^{>}!}{n_{op}^{<}!}}\right) \tag{23}$$

for $s_{ip/op} = 0, \pm 1$, and zero otherwise. For resolved sideband PRS, the starting point is normally to have both motional modes cooled to the quantum mechanical ground state. Eq. (23) is then typically a good approximation for simulating the internal and external quantum dynamics before the final unresolved sideband detection addressing the $|g_r\rangle$ - $|f_r\rangle$ transition of the readout ion (step iv), Fig. 1). This readout signal corresponds to a projection measurement of the readout ion to its ground state $|g_r, i_t, n_{ip}, n_{op}\rangle$. Formally, it is proportional to

$$P_{|g_r\rangle} = \sum_{n_{ip},n_{op},i_t} |\langle\psi_{\mathrm{Ham}}|g_r, i_t, n_{ip}, n_{op}\rangle|^2, \tag{24}$$

with $\psi_{\mathrm{Ham}}$ being the wavefunction after the Hamiltonian evolution of steps i) to iii) of the PRS sequence.

### *2.2. PRS in the unresolved sideband regime*

Although PRS was originally developed for ultra-precise spectroscopy in the resolved sideband regime, PRS in unresolved sideband scenarios can as well be interesting for a range of investigations of molecules in the gas phase. This includes internal state preparation, broad line absorption spectroscopy under diverse but well-controlled conditions, and single photon absorption studies of non- or weakly-fluorescing molecules. The unresolved sideband PRS scenario appears naturally in two generic cases: when the motional sideband frequencies of the two-ion system are either smaller than or similar to: 1) the natural linewidth of the spectroscopic transition, or 2) the linewidth of the applied light source. In general, to simulate the photon recoil spectrum under such circumstances, one has to solve the very complicated master equations [26] based on the theory presented in Sec. 2.1 but including the laser linewidth and/or the natural linewidth of the addressed transition. However in the following, we will take a simpler approach which should be valid in the limit of no remaining coherence in the interaction with the light field. The internal state evolution can then be described by excitation and de-excitation rates in accordance with Einstein's theory for light absorbers interacting with broadband (blackbody) fields [27]. We will further assume that the wave vectors of the absorbed and emitted photons can all be represented by the one corresponding to that of the transition center (i.e. assuming the transition linewidth to be much narrower than the transition frequency). We can then apply Eq. (20) using a single value of $\|\vec{k}_L\|$ (or $\|\vec{k}_{spon}\|$ for spontaneous emission) to evaluate the relative coupling between motional states. Based on these approximations, we can now formally write up rate equations governing the dynamics of the internal and external

state populations as

$$\begin{aligned}\frac{d}{dt}P_{|i_r,g_t,n_{ip},n_{op}\rangle} = \sum_{s_{ip},s_{op}} & -R_{\text{abs}}(n_{ip},n_{op},s_{ip},s_{op})P_{|i_r,g_t,n_{ip},n_{op}\rangle} \\ & + [R_{\text{stim}}(n_{ip},n_{op},s_{ip},s_{op}) \\ & + R_{\text{spon}}(n_{ip},n_{ip},s_{ip},s_{op})]P_{|i_r,e_t,(n_{ip}+s_{ip}),(n_{op}+s_{op})\rangle} \\ & - (R_{H,ip}+R_{H,op})P_{|i_r,g_t,n_{ip},n_{op}\rangle} \\ & + R_{H,ip}P_{|i_r,g_t,(n_{ip}-1),n_{op}\rangle} \\ & + R_{H,op}P_{|i_r,g_t,n_{ip},(n_{op}-1)\rangle}\end{aligned} \tag{25}$$

$$\begin{aligned}\frac{d}{dt}P_{|i_r,e_t,n_{ip},n_{op}\rangle} = \sum_{s_{ip},s_{op}} & -[R_{\text{stim}}(n_{ip}-s_{ip},n_{op}-s_{op},s_{ip},s_{op}) \\ & + R_{\text{spon}}(n_{ip}-s_{ip},n_{op}-s_{op},s_{ip},s_{op})]P_{|i_r,e_t,n_{ip},n_{op}\rangle} \\ & + R_{\text{abs}}(n_{ip}-s_{ip},n_{op}-s_{op},s_{ip},s_{op})P_{|i_r,g_t,(n_{ip}-s_{ip}),(n_{op}-s_{op})\rangle} \\ & - (R_{H,ip}+R_{H,op})P_{|i_r,e_t,n_{ip},n_{op}\rangle} \\ & + R_{H,ip}P_{|i_r,e_t,(n_{ip}-1),n_{op}\rangle} \\ & + R_{H,op}P_{|i_r,e_t,n_{ip},(n_{op}-1)\rangle}\end{aligned} \tag{26}$$

for the target ion being in the internal ground or excited state respectively. Here, $R_{\text{abs/stim}}(n_{ip},n_{op},s_{ip},s_{op})$ describe the rates of photon absorption and stimulated emission, and can be expressed as:

$$\begin{aligned}R_{\text{abs/stim}}(n_{ip},n_{op},s_{ip},s_{op}) &= B_{\text{abs/stim}} \times \rho_{\text{eff}}(\omega_t,\omega_L) \times |\xi(n_{ip},n_{op},s_{ip},s_{op})|^2 \\ &= R_{\text{abs/stim},0}(\omega_t,\omega_L) \times |\xi(n_{ip},n_{op},s_{ip},s_{op})|^2\end{aligned} \tag{27}$$

with

$$B_{\text{stim}} = \frac{\pi^2 c^3}{\hbar\omega_t^3}\Gamma_t, \quad B_{\text{abs}} = B_{\text{stim}}, \tag{28}$$

$\Gamma_t$ being the spontaneous decay rate of the transition. $\rho_{\text{eff}}(\omega_t,\omega_L)$ denotes the effective spectral energy density at the transition frequency $\omega_t$ due to a laser line centered around $\omega_L$. Generally, we can write $\rho_{\text{eff}}(\omega_t,\omega_L)$ as

$$\rho_{\text{eff}}(\omega_t,\omega_L) = \frac{3I_L}{c}\int_{-\infty}^{\infty} L_t(\omega',\omega_t)L_L(\omega',\omega_L)\,d\omega', \tag{29}$$

where $I_L$ denotes the total intensity of the laser beam and $L_t(\omega,\omega_t)$ and $L_L(\omega,\omega_L)$ represent the line shape functions for the target ion transition and laser field respectively. The factor of 3 in this formula is introduced because we consider here, in contrast to the original scenario considered by Einstein of classical electric dipoles interacting with unpolarized and randomly propagating electromagnetic fields, a laser field with a well-defined polarization and an aligned induced electric dipole by construction. We

assume the laser field to have a Gaussian[1] frequency distribution with a full width at half maximum (FWHM) $\Gamma_L \equiv \sqrt{8\ln(2)}\sigma_L$ (where $2\sigma_L$ is the full width at $1/\sqrt{e}$), and the target transition to be Lorentzian[2] and governed by the natural decay rate $\Gamma_t$. The two line shapes can be written as

$$L_L(\omega, \omega_L) = \frac{1}{\sqrt{2\pi}\sigma_L} e^{\frac{-(\omega-\omega_L)^2}{2\sigma_L^2}} \tag{30}$$

and

$$L_t(\omega, \omega_t) = \frac{1}{\pi} \frac{\Gamma_t/2}{(\omega-\omega_t)^2 + \Gamma_t^2/4}. \tag{31}$$

In Sec. 3 we will consider two specific cases where either $\Gamma_L \ll \Gamma_t$ or $\Gamma_L \gg \Gamma_t$ in which cases $\rho_{\text{eff}}(\omega_t, \omega_L)$ reduces to

$$\rho_{\text{eff}}^t(\omega_t, \omega_L) = \frac{3I_L}{c} L_t(\omega_L, \omega_t) \tag{32}$$

and

$$\rho_{\text{eff}}^L(\omega_t, \omega_L) = \frac{3I_L}{c} L_L(\omega_t, \omega_L), \tag{33}$$

respectively. It is obvious from Eq. (27) that we have the largest absorption and stimulated emission rates when $\omega_L = \omega_t$, which leads to, for the two cases of $\Gamma_L \ll \Gamma_t$ and $\Gamma_L \gg \Gamma_t$, the following values for $R_{\text{abs/stim},0}(\omega_t, \omega_L)$:

$$\begin{aligned} R_{\text{abs/stim},0}^t(\omega_t, \omega_t) \equiv R_{\text{abs},0}^{\text{res},t} &= \frac{6\pi c^2}{\hbar\omega_t^3} I_L \\ &\equiv \Gamma_t \frac{I_L}{I_{\text{sat}}^t}, \qquad I_{\text{sat}}^t \equiv \frac{\hbar\omega_t^3\Gamma_t}{6\pi c^2} \end{aligned} \tag{34}$$

and

$$\begin{aligned} R_{\text{abs/stim},0}^L(\omega_t, \omega_t) \equiv R_{\text{abs},0}^{\text{res},L} &= \frac{3\pi^{3/2}c^2}{\sqrt{2}\hbar\omega_t^3} \frac{\Gamma_t}{\sigma_L} I_L \\ &\equiv \Gamma_t \frac{I_L}{I_{\text{sat}}^L}, \qquad I_{\text{sat}}^L \equiv \frac{\sqrt{2}\hbar\omega_t^3\sigma_L}{3\pi^{3/2}c^2}, \end{aligned} \tag{35}$$

respectively. Here, the intensity $I_{\text{sat}}$ is defined in both cases as the laser intensity which leads to an excitation rate $R_{\text{abs},0}^{\text{res}}$ equal to $\Gamma_t$.

Regarding the contribution of spontaneous emission to Eq. (25)-(26), one has to scale the rate $\Gamma_t$ with a factor accounting for the average probability to emit on a certain sideband. This factor depends on the spatial emission pattern of the specific transition. If we define $\theta \in [0, \pi]$ as the angle between the spontaneously emitted

[1]This laser lineshape is chosen as an example since it is common, but any lineshape can be considered.

[2]Typical for the natural lineshape of a transition, but it could have a different shape if other processes than spontaneous emission play a significant role.

photon wave vector $\vec{k}_{spon}$ and the $z$-axis, and $\phi \in [0, 2\pi]$ as the angle between the $y$-axis and the projection of $\vec{k}_{spon}$ on the $xy$-plane, we can write

$$\frac{\vec{k}_{spon}}{\|\vec{k}_{spon}\|} = \begin{pmatrix} \sin\theta\cos\phi \\ \sin\theta\sin\phi \\ \cos\theta \end{pmatrix}. \tag{36}$$

In spherical coordinates, we can then write the spontaneous emission rate as

$$R_{\text{spon}}(n_{ip}, n_{op}, s_{ip}, s_{op}) = \Gamma_t D_{n_{ip},n_{op},s_{ip},s_{op}} \tag{37}$$

with

$$D_{n_{ip},n_{op},s_{ip},s_{op}} = \int d\Omega |\xi(\eta_{ip,t}(\theta), \eta_{op,t}(\theta), n_{ip}, n_{op}, s_{ip}, s_{op})|^2 W(\theta,\phi), \tag{38}$$

where $\vec{k}_L$ must be replaced by $\vec{k}_{spon}$ in eq. (9) for $\eta_{ip/op,t}$. The emission pattern $W(\theta,\phi)$ is the probability that the spontaneously emitted photon propagates along the $(\theta,\phi)$ direction.

Finally, for realistic simulation of the PRS spectra, one has to take into account heating of the motional modes due to imperfect trapping conditions. The associated heating rates can be very mode-dependent but are typically independent of the internal state of the two ions as well as on the specific mode excitation [19]. They are introduced in Eq. (25)-(26) by the terms containing the rates $R_{H,ip/op}$.

Although the spectroscopy laser does not exclusively address the first BSB as in the case of resolved sideband PRS (it actually addresses many sidebands simultaneously), light-ion interaction still leads to excitation of both motional modes according to Eq. (25)-(26). The resulting motional state populations depend on the transition line profile, the laser parameters (intensity, central frequency and linewidth) as well as the time the laser light is applied.

A signal reflecting the motional mode distribution can be obtained by applying to the readout ion a sideband resolved shelving pulse of length $\tau_r$ with respect to one of the two modes (assuming no other sidebands nor the carrier transition are driven). The probability for the readout ion to be shelved in the $|e_r\rangle$ state is given by

$$P_{|e_r\rangle}(\tau_r, \Delta_r) = \sum_{n_{ip},n_{op}} \frac{\Omega^2_{n_{ip},n_{op},s_{ip},s_{op}}}{\Delta_r^2 + \Omega^2_{n_{ip},n_{op},s_{ip},s_{op}}} \sin^2\left(\sqrt{\Delta_r^2 + \Omega^2_{n_{ip},n_{op},s_{ip},s_{op}}}\frac{\tau_r}{2}\right) P_{|g_r,i_t,n_{ip},n_{op}\rangle} \tag{39}$$

with $\Delta_r = \omega_L - (\omega_r + s_{ip}\omega_{ip} + s_{op}\omega_{op}) = \delta_r - (s_{ip}\omega_{ip} + s_{op}\omega_{op})$ being the detuning from the sideband in question. For $\Delta_r = 0$, the probability to stay in the ground state $|g_r\rangle$ when addressing the 1st RSB of the OP mode is then

$$P_{|g_r\rangle}(\tau_r) = 1 - \sum_{n_{ip},n_{op}} \sin^2\left(\Omega_{n_{ip},n_{op},s_{ip}=0,s_{op}=-1} \times \frac{\tau_r}{2}\right) P_{|g_r,i_t,n_{ip},n_{op}\rangle} \tag{40}$$

where $\Omega_{n_{ip},n_{op},s_{ip}=0,s_{op}=-1}$ indicates the Rabi angular frequency of the 1st RSB transition for a given motional state. As mentioned previously (see Eq. 24), the readout fluorescence signal during step iv) is directly proportional to $P_{|g_r\rangle}$. Clearly, if there is

no motional excitation by the spectroscopy laser, there is also no excitation by the resolved RSB laser pulse since $P_{|e_r\rangle} = 0$ for $n_{ip} = n_{op} = 0$ (assuming no heating from other sources), and the readout ion fluoresces when finally driving the $|g_r\rangle - |f_r\rangle$ transition. Conversely, any excitation by the spectroscopy laser pulse leads to a reduced fluorescence signal. As is evident from Eq. (40), the fluorescence reduction also depends on the duration of the resolved RSB pulse, which in the following is chosen to be $\tau_r = \pi/\Omega_{n_{ip}=0,n_{op}=1,s_{ip}=0,s_{op}=-1}$. In the following sections we will present simulation results for the kind of PRS spectra one obtains in the non-resolved sideband scenarios.

## 3. Simulations of unresolved photon recoil spectra

In this section, we present simulated unresolved PRS spectra, where either the natural linewidth of the transition (Sec. 3.1) or the linewidth of the laser (Sec. 3.2) dominates the dynamics. More specifically, in Sec. 3.1, we consider PRS of the rather broad 3s $^2S_{1/2}$ 3p $^2P_{3/2}$ electronic transition ($\Gamma_t/2\pi = 41.8(4)\,\mathrm{MHz}$) of a single $^{24}Mg^+$ ion at $\lambda = 279.6$ nm by a narrow laser source ($\Gamma_L/2\pi \lesssim 1\,\mathrm{MHz} \ll \Gamma_t/2\pi$). Section 3.2 is devoted to simulation of mid-infrared vibrational PRS spectra of the very narrow $|\nu = 0, J = 1\rangle - |\nu' = 1, J' = 0\rangle$ closed transition ($\Gamma_t/2\pi = 2.50$ Hz) at $\lambda = 6.17\,\mu\mathrm{m}$ in the $^1\Sigma^+$ electronic ground state of $^{24}MgH^+$ by a laser source with a linewidth varying from $\Gamma_L/2\pi \sim 10$ to 100 MHz.

### *3.1. Simulation of unresolved PRS due to transition line broadening*

In this section we simulate the PRS of the rather broad 3s $^2S_{1/2}$ - 3p $^2P_{3/2}$ electronic transition ($\Gamma_t/2\pi = 41.8(4)\,\mathrm{MHz}$) of a single $^{24}Mg^+$ ion at $\lambda = 279.6$ nm (See Fig. 2a) by a laser source with such a narrow linewidth ($\Gamma_L \ll \Gamma_t$) that we disregard it. Applying linearly polarized spectroscopic laser light along a biais magnetic field axis (y-axis), only two sub-level transitions $^2S_{1/2}$ ($m_J = \pm 1/2$) - $^2P_{3/2}$ ($m_J = \pm 1/2$) can be excited with equal strength (see Fig. 2b). Furthermore, since the spontaneous emission pattern from the $^2P_{3/2}$ ($m_J = \pm 1/2$) sub-states have identical effects on the motional mode excitations, the two transitions are identical from an excitation and spontaneous emission point of view, and the dynamics is equivalent to the one of a two-level system. The effective saturation intensity is however 1.5 times larger than in the two-level theory presented in Sec. 2 due to the square of the Clebsch-Gordan coefficient being 2/3. In the simulations this has been implemented by multiplying $R^{\mathrm{res}}_{\mathrm{abs},0}$ from Eq. (34) by 2/3. We furthermore assume that the $^{24}Mg^+$ target ion is sympathetically cooled to the motional ground state of both modes by a directly sideband-cooled readout $^{40}Ca^+$ ion.

#### *3.1.1. Absorption and stimulated emission*

Assuming $\omega_z = 2\pi \times 147.9\,\mathrm{kHz}$ for a single $^{40}Ca^+$ ion, we get from Eq. (4) $\omega_{ip} = 2\pi \times 162.9\,\mathrm{kHz}$ and $\omega_{op} = 2\pi \times 300.2\,\mathrm{kHz}$. Both mode angular frequencies are more than two orders of magnitude smaller than $\Gamma_t$. Hence, we are clearly in the regime where we can apply Eqs. (25)-(26) with Eq. (32). With $\lambda_t = 279.6\,\mathrm{nm}$ for the target ion and the above mode angular frequencies, the LDPs for absorption and spontaneous emission are $\eta_{ip,t} = 0.42$ and $\eta_{op,t} = 0.51$ for the spectroscopy laser beam propagating along the $z$-axis. In the simulations to be presented below, we will, however, use the values $\eta_{ip,t} = 0.30$ and $\eta_{op,t} = 0.36$ in order to compare the results with recent

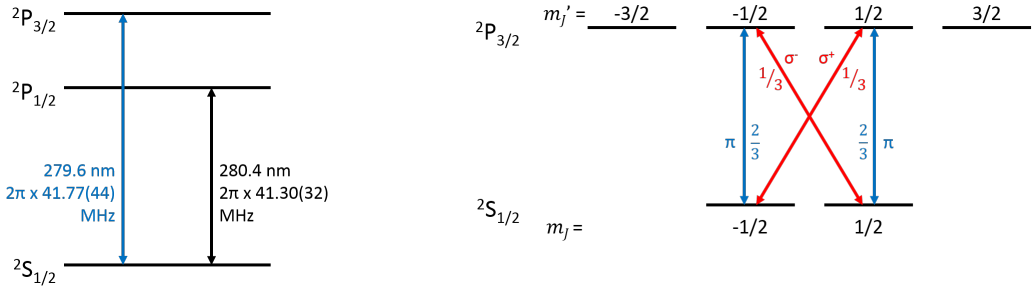


**Figure 2.** (a) Energy levels of $^{24}Mg^+$. The 3s $^2S_{1/2}$ - 3p $^2P_{3/2}$ transition is the one used for spectroscopy in our simulations and experiments. (b) The energy levels of $^{24}Mg^+$ have sub-levels which are degenerate in the presence of a magnetic field. $\pi$-transitions do not change the secondary total angular momentum $m_J$ whereas $\sigma$ transitions change it by $\pm 1$. The norm squared values of the Clebsch-Gordan coefficients associated with these transitions are shown.

experiments where the $^{24}Mg^+$ spectroscopy laser beam is making a 45° angle with the $z$-axis, reducing the LDPs by a factor $\sqrt{2}$. While this approach gives the correct effect of the momentum recoil along the $z$-axis with respect to absorption and stimulated emission, it neglects the effect of motional excitations in the plane perpendicular to the $z$-axis. In the present unresolved sideband PRS situation, it is merely expected to lead to slightly reduced induced transition rates and a minor Doppler broadening of the target line (See details in Sec. 3.1.7).

### *3.1.2. Spontaneous emission*

To simulate the effect of spontaneously emitted photons following Eq. (37-38), we must know the emission pattern of the specific transition. To determine that, we have to take into account the particular Zeeman sub-level structure of the 3s $^2S_{1/2}$ - 3p $^2P_{3/2}$ electronic transition in the $^{24}Mg^+$ ion and the relative branching ratios between sub-level transitions given by the square of the Clebsch-Gordan coefficients (See Fig. 2b). With respect to the chosen spherical coordinate system described in connection with Eq. (36), the spontaneous emission pattern is given by

$$W(\theta,\phi) = \frac{2}{3}W_\pi(\theta,\phi) + \frac{1}{3}W_\sigma(\theta,\phi), \tag{41}$$

where

$$\begin{aligned} W_\pi(\theta,\phi) &= \frac{3}{8\pi}\sin^2(\arccos(\sin\theta\sin\phi)) \quad \text{and} \\ W_\sigma(\theta,\phi) &= \frac{3}{16\pi}(1+\sin^2\theta\sin^2\phi) \end{aligned} \tag{42}$$

are the individual emission patterns of the two possible types of sub-level transitions, $\pi$ ($\Delta m_J = 0$) and $\sigma$ ($\Delta m_J = \pm 1$) respectively (see Ref. [28] pp. 550-530).

### *3.1.3. Basis for the numerical simulations*

In the following simulations, we will assume the target and readout ions to be in the $|g_t\rangle$ and $|g_r\rangle$ states respectively and both the motional modes cooled to their ground state (i.e. $n_{ip} = 0$ and $n_{op} = 0$). In order to perform the simulations in a reasonable time

on a standard personal computer, we have limited the motional state basis to a grid corresponding to $n_{ip} = 0-19$ and $n_{op} = 0-19$ (400 states in total). Consequently, the population will eventually be moved outside the state space for long spectroscopy pulse times. For the present calculations the amount of population outside the state space has been limited to 1%, effectively limiting the duration of the dynamics evolution we can simulate. Based on Eq. (20) which represents the relative coupling strengths of the various sidebands, we have found that it suffices to take into account sidebands up to $s_{ip,max} = \pm 5$ and $s_{op,max} = \pm 6$. Based on trap heating rate measurements, we take $R_{H,ip} = 14(1)\,\mathrm{s}^{-1}$ and $R_{H,op} = 1.7(3)\,\mathrm{s}^{-1}$.

### *3.1.4. Simulations of the dynamics of motional state populations on resonance*

In the present case, we consider the limit where $\Gamma_L \ll \Gamma_t$. From Eq. (34), the saturation intensity is $I^t_{sat} = 0.749\,\mathrm{W\,cm^{-2}}$. For laser intensities $I_L \ll I^t_{sat}$, we cannot ignore the spontaneous emission terms of Eqs. (25-26), while in the case of $I_L \gg I^t_{sat}$, the spontaneous emission terms can effectively be neglected. In the latter case, when the trap heating rates can also be ignored, all terms on the right hand side of Eqs. (25-26) are proportional to $R^{\mathrm{res,t}}_{\mathrm{abs},0}$ and the dynamics should have exactly the same behavior when the spectroscopy pulse time is scaled by this factor. To express this we define $\tau_{scaled} \equiv \tau_{spec} \times R^{\mathrm{res},t}_{\mathrm{abs},0}$, which is roughly proportional to the number of scattered photons from the laser beam.

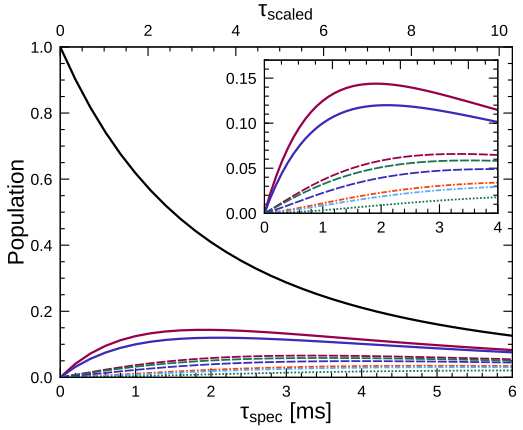


**Figure 3.** Simulated evolution of the population in different motional states as a function of spectroscopy pulse time $\tau_{\mathrm{spec}}$ (bottom axis) and scaled time $\tau_{\mathrm{scaled}}$ (top axis) for a laser on resonance ($\omega_L = \omega_t$) and with $I_L = 4.9\,\mu\mathrm{W\,cm^{-2}} = 6.54 \times 10^{-6} I^t_{\mathrm{sat}}$. The following notation refers to motional states $(n_{ip}, n_{op})$: (0,0) ━━, (0,1) ——, (1,0) ——, (0,2) - - -, (1,1) - - -, (2,0) - - -, (1,2) -·-·-, (2,1) -·-·-, (2,2) ·····.

In Fig. 3, we show the temporal evolution of the population of the various motional states $(n_{ip},\ n_{op})$ from solving Eqs. (25-26) assuming $\omega_L = \omega_t$ and for $I_L = 6.54 \times 10^{-6} I^t_{sat}$. This intensity is chosen to compare with experimental results presented in sub-section 3.1.7. More specifically, the figure shows the populations versus real time $\tau_{spec}$ (bottom x-axis) as well as the scaled time $\tau_{scaled}$ (top x-axis). As evident from this figure, the motional ground state population (0,0) is a monotonically decreasing function of time. At short times, the populations of all other motional states $(n_{ip}, n_{op}) \neq (0,0)$ increase linearly with time as expected for rate equations. For longer times, the populations saturate and eventually decrease as a broader range of motional

states is reached.

### *3.1.5. Simulation of motional population spectra*

Scanning the laser frequency $\omega_L$ across the resonance of the target ion transition for a fixed interaction time leads to what we name the motional population spectra. In Fig. 4, we present such spectra for $I_L = 6.54 \times 10^{-6} I_{sat}^t$ and for spectroscopy times $\tau_{spec} = 1.3\,\text{ms}$ and 5.3 ms ($\tau_{scaled} = 2.23$ and 9.10). For these parameters, one clearly sees the effect of population depletion of the lower excited motional states around the resonance due to the effective motional state spreading. Only for the weakly populated states, a normal spectral response with a width reflecting the natural linewidth of the transition is observed. For PRS one has, however, to be aware that the motional spectra presented in Fig. 4 will not be read out individually by the readout procedure (steps iii) and iv)) reported previously. This readout signal is instead an intricate combination of contributions from each of the motional population spectra, as will be discussed in the following sub-section.

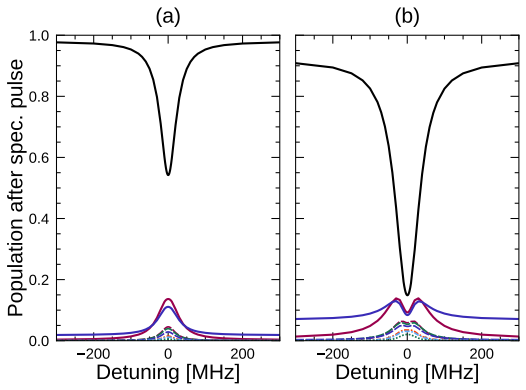


**Figure 4.** Simulated population in different motional states after a spectroscopy pulse of length $\tau_{\text{spec}} = 1.3$ ms ($\tau_{\text{scaled}} = 2.23$) **(a)** and 5.3 ms ($\tau_{\text{scaled}} = 9.10$) **(b)** as a function of spectroscopy laser detuning for a spectroscopy laser intensity of $I_L = 4.9\,\mu\text{W}\,\text{cm}^{-2} = 6.54 \times 10^{-6} I_{\text{sat}}^t$. The following notation refers to motional states $(n_{ip}, n_{op})$: (0,0) ——, (0,1) ——, (1,0) ——, (0,2) - - -, (1,1) - - -, (2,0) - - -, (1,2) -·-·-, (2,1) -·-·-, (2,2) ·····.

### *3.1.6. Simulation of readout spectra*

To simulate the PRS spectrum, one first has to solve the time dependent Schrödinger equation Eq. (17) in the $|i_r, i_t, n_{ip}, n_{op}\rangle$ basis when addressing the readout ion on a specific red sideband transition. The coupling matrix elements are given by Eq. (18) and the initial state is the mixed state resulting from the rate equation dynamics presented in the previous sub-section. Since the fluorescence signal is sideband unresolved and hence essentially just proportional to $P_{|g_r\rangle}$, it corresponds in the simulation to projecting the final state $|\psi\rangle$ on the $|g_r, i_t, n_{ip}, n_{op}\rangle$ states as described by Eq. (24) and (40).

In Fig. 5, we show the norm of such projections corresponding to the two population spectra in Fig. 4 after applying a readout pulse on the $^{40}Ca^+$ ion. More specifically, this pulse corresponds to a $\pi$-pulse with respect to the (0,1) $\rightarrow$ (0,0) 1st RSB of the 4s $^2S_{1/2}$ - 3d $^2D_{5/2}$ quadrupole transition. With a transition wavelength of 729 nm and the mode frequencies given above, we get $\eta_{ip,r} = 0.204$ and $\eta_{op,r} = 0.0917$. A bit surprisingly, the fluorescence spectrum in Fig. 5b shows no sign of the depletion around

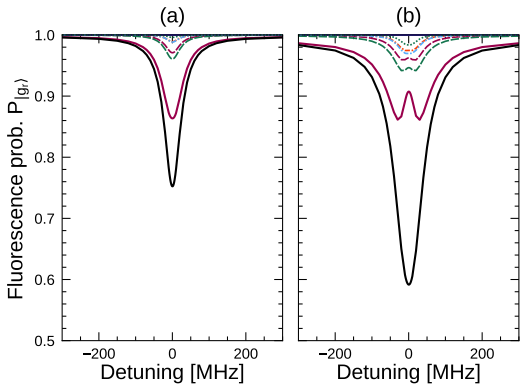


**Figure 5.** Simulated fluorescence probability $P_{|g_r\rangle}$, ▬, corresponding to the detected signal, for spectroscopy pulse lengths of $\tau_{\rm spec} = 1.3$ ms ($\tau_{\rm scaled} = 2.23$) **(a)** and 5.3 ms ($\tau_{\rm scaled} = 9.10$) **(b)** as a function of spectroscopy laser detuning for a spectroscopy laser intensity of $I_L = 4.9\,\mu{\rm W\,cm^{-2}} = 6.54 \times 10^{-6} I^t_{\rm sat}$. The other curves are the contributions from different motional states, corresponding to the terms in the sum of Eq. (40). The following notation refers to motional states $(n_{ip}, n_{op})$: (0,1) ▬, (1,1) ▬, (2,1) ▬, (0,2) ▬, (1,2) ▬, (2,2) ▬.

resonance seen in the corresponding population spectrum presented in Fig 4b. This is because the many small contributions from non-depleted higher motional states "fill out the dip".

It is clear from Fig. 5 that there is a spectral broadening and an increase in signal depth with $\tau_{spec}$ for a fixed $R^{{\rm res},t}_{{\rm abs},0}$. However, the spectroscopic signal does not significantly change as long as $\tau_{\rm scaled}$ is constant. This can be seen in Fig. 6 showing the signal FWHM and depth as a function of $\tau_{\rm scaled}$ for various laser intensities. The values have been extracted by fitting signal peaks with a Lorentzian function. The slight discrepancies between the different lines are due to trap heating which, as expected, is almost negligible for the $^{24}{\rm Mg}^+$ case. Indeed, trap heating plays a role only for very weak laser intensities for which the light induced rate out of the motional ground state is reduced to the order of the trap heating.

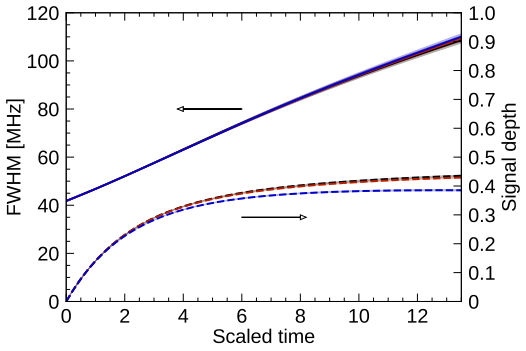


**Figure 6.** FWHM (left axis solid curves) and signal depth (right axis dashed curves) of simulated fluorescence curves fitted to a Lorentzian function vs. scaled time for 3 different spectroscopy laser intensities $I_L = 1\,\mu{\rm W\,cm^{-2}} = 1.34 \times 10^{-6} I^t_{\rm sat}$ (▬), $I_L = 5\,\mu{\rm W\,cm^{-2}} = 6.68 \times 10^{-6} I^t_{\rm sat}$ (▬), and $I_L = 15\,\mu{\rm W\,cm^{-2}} = 2.00 \times 10^{-5} I^t_{\rm sat}$ (▬). The lighter colored shadows around the lines represent the standard deviation from the Lorentzian fits. The deviation in signal depth for the different intensities is caused by heating from noise, which influences low intensities more due to lower $R^{\rm res}_{{\rm abs},0}$ values.

The FWHM at scaled times $\tau_{\rm scaled} \to 0$ has the expected value of the transition linewidth and increases almost linearly with $\tau_{\rm scaled}$. This is because the signal relies on

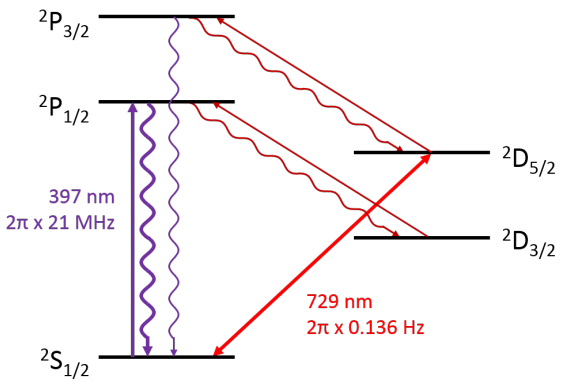


**Figure 7.** Energy levels and electronic transitions of the $^{40}Ca^+$ readout ion relevant to laser cooling and resolved sideband spectroscopy.

the depletion of the motional ground state. Even at large detunings, there is still a small probability to excite the transition and to move population out of the motional ground state. The probability for each detuning increases with $\tau_{\text{scaled}}$, but eventually saturates when all the population is moved out. As $\tau_{\text{scaled}}$ keeps increasing, depletion of the motional ground state happens for a broader and broader frequency span around the resonance, and thus the signal width increases indefinitely. This depletion effect also causes the observed signal depth saturation for high $\tau_{\text{scaled}}$. Indeed, for very long $\tau_{\text{scaled}}$ the population is spread out over many motional states from where the probability to not be shelved by the readout pulse is governed by Eq. (40). In the limit where all the population is in many very high motional states, $P_{|g_r\rangle} \to 1/2$ (the average value of a $\sin^2(x)$ function). The signal depth can be 1 only in the resolved PRS regime, where the motional ground state population is coherently driven to one specific excited motional state.

### *3.1.7. Comparison with experimentally obtained spectra*

The experiments are initialized by sideband cooling a single $^{24}Mg^+$ and a single $^{40}Ca^+$ ion to the ground state with respect to both the IP and OP modes. Sideband cooling is done by addressing the 4s $^2S_{1/2}$ - 3d $^2D_{5/2}$ quadrupole transition of the $^{40}Ca^+$ ion (See Fig. 7). The IP and OP mode angular frequencies are $\omega_{ip} = 2\pi \times 162.9\,\text{kHz}$ and $\omega_{op} = 2\pi \times 300.2\,\text{kHz}$ respectively. A typical sideband excitation spectrum on the $^{40}Ca^+$ quadrupole transition after sideband cooling is presented in Fig. 8. A fit to the experimental data points leads to mean occupation numbers of $\langle n_{ip}\rangle = 0.09(+0.18 - 0.09)$ and $\langle n_{op}\rangle = 0.14(+0.24 - 0.14)$ for the IP and OP modes respectively. The laser beam exciting the $^{24}Mg^+$ ion makes a 45° angle with the $z$-axis. Its polarization is linear and aligned with the $y$-axis along which a weak magnetic bias field (6.523(3) G) is also pointing.

Experimentally obtained PRS spectra of the 3s $^2S_{1/2}$ - 3p $^2P_{3/2}$ transition in $^{24}Mg^+$ are presented in figure 9.a). In the experiments we used $I_L = 4.9(7)\,\mu\text{W}\,\text{cm}^{-2} = 6.5(9) \times 10^{-6} I^t_{\text{sat}}$ and, from left to right, spectroscopy excitation times of $\tau_{spec} = 1.3(1)$, 3.6(1) and 5.3(1) ms. All three experimental spectra have been centered at a detuning of 0 MHz, while the wavelength meter readings gave offsets of 12(4) MHz, 11(2) MHz and 18(3) MHz respectively, compared to the most precisely measured value of the transition [14]. These discrepancies are however all within the accuracy

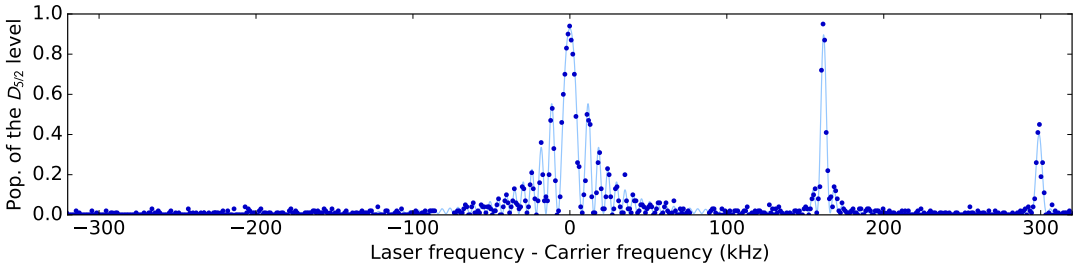


**Figure 8.** Resolved sideband spectrum representing the probability of excitation of the $3s^2S_{1/2}$ - $3p^2D_{5/2}$ of $^{40}Ca^+$ as a function of the 729 nm laser's detuning with respect to the carrier transition. This spectrum was obtained after Doppler cooling followed by sideband cooling. The absence of visible red sidebands indicates a high probability of occupation of the ground state for both motional modes. The duration and intensity of the 729 nm probe pulse were chosen to perform a $\pi$-pulse on the first blue sideband of the in-phase mode at 162.9 kHz. The blue line is a fit to the data points and gives mean occupation numbers of $\langle n_{ip}\rangle = 0.09(+0.18-0.09)$ and $\langle n_{op}\rangle = 0.14(+0.24-0.14)$ for the in-phase and out-of-phase modes respectively.

of the wavelength meter (HighFinesse Ångstom WS-U). Figures 9.b) and 9.c) show, together with simulation results, the evolution of the measured spectral depth and width as a function of spectroscopy time $\tau_{spec}$. There is a fairly good agreement between experiments and simulations within the error bars. The black dashed line in figure 9.c) represents the natural FWHM of the transition ($\Gamma_t/2\pi = 41.8(4)$ MHz). The black dotted line represents the effective FWHM which is slightly broader due to two effects. First, the finite temperature ($\sim 0.75$ mK) of the ions perpendicular to the $z$-axis leads to a Doppler broadening in the direction of the applied spectroscopic laser beam. This broadening is about $\Delta\omega_{Dopp} \sim 2\pi \times 3$ MHz and is common to each of the two ($m_J = \pm 1/2$) - ($m_J = \pm 1/2$) sub-level transitions. Second, the applied weak magnetic field gives rise to a differential Zeeman shift of the two sub-level transitions of $\Delta\omega_{Zee} = 2\pi \times 6.1$ MHz. By simulating the effective line profile of the transition taking both effects into account, we find an effective FWHM of about 42.5 MHz. A linear fit of the experimental data gives a FWHM at zero spectroscopy time of 35(9) MHz (green line figure 9.c)). Although not a precision measurement, this result matches well the effective FWHM of the transition.

Since the IP and OP modes get similarly excited during the spectroscopy phase, as is clear from Fig. 3, the spectroscopic signal strength might actually be increased significantly by addressing both modes consecutively in the readout phase. This scenario can be realized by consecutively applying $\pi$-pulses on the (0,1) $\rightarrow$ (0,0) and (1,0) $\rightarrow$ (0,0) sidebands, with respect to two different sub-level transitions (e.g. the $m_J = -1/2 \rightarrow m_{J'} = -5/2$ and $m_J = -1/2 \rightarrow m_{J'} = -3/2$ transitions). In the case of $^{40}Ca^+$ being the readout ion, one can in principle sequentially address up to four sub-level transitions (e.g. $m_J = -1/2 \rightarrow m_{J'} = -5/2, -3/2, 1/2, 3/2$) by different orders of red sideband pulses for both motional modes, and in this way increase the spectroscopy signal even further. However, the total time needed to perform coherent manipulations during the readout phase will increase and heating of the motional modes due to imperfect trapping conditions will eventually limit this strategy. For short excitation times, applying consecutive $\pi$-pulses on the (0,1) $\rightarrow$ (0,0) and (1,0) $\rightarrow$ (0,0) sideband transitions will often be an advantage. In Fig. 10, we present experimental PRS spectra when addressing either only the (0,1) $\rightarrow$ (0,0) sideband or both the (0,1) $\rightarrow$ (0,0) and (1,0) $\rightarrow$ (0,0) sidebands. In this particular case, one clearly sees the gain in signal strength in the two $\pi$-pulse scheme. In the experiment, we used

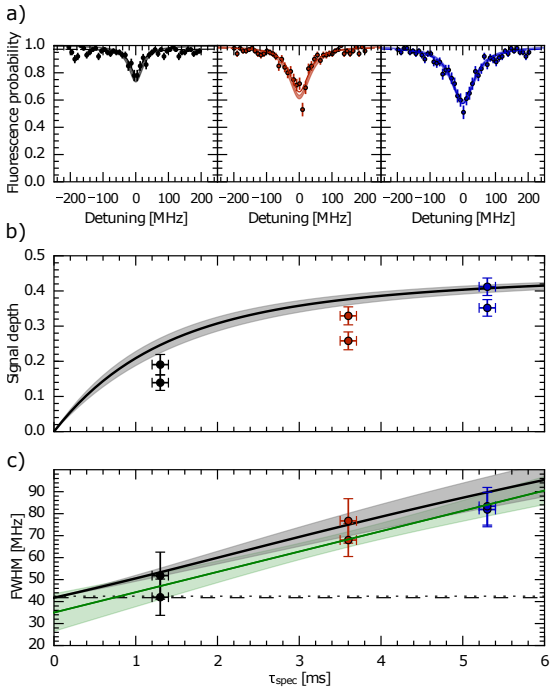


**Figure 9.** Unresolved sideband photon-recoil spectroscopy of the 3s $^2S_{1/2}$ - 3p $^2P_{3/2}$ transition in the $^{24}Mg^+$ ion with a single co-trapped $^{40}Ca^+$ ion as the readout ion. a) Typical experimental spectra obtained for a spectroscopy laser intensity of $I_L = 4.9(7)\,\mu W\,cm^{-2} = 6.5(9) \times 10^{-6} I^t_{sat}$ and, from left to right, spectroscopy times of 1.3(1) ms, 3.6(1) ms and 5.3(1) ms ($\tau_{scaled}$ = 2.2, 6.2, and 9.1). The lighter colored broader lines represent the simulated results when including the $1\sigma$-uncertainty on the experimental value of $I_L$. The dashed lines are Lorentzian fits to the experimental data from which the signal depths and full widths at half maximum (FWHM) are extracted. b) Extracted signal depth as a function of spectroscopy time together with simulated values for $I_L = 4.9\,\mu W\,cm^{-2}$ (black line) including the $1\sigma$-uncertainty on $I_L$ (gray shaded area). c) Extracted FWHM as a function of spectroscopy time together with the simulated values (black line). A linear fit of the experimental data is also shown in green together with the resulting one standard deviation of the fit (green shaded area). The intercept at zero spectroscopy time of 35(9) MHz matches the expected FWHM (dotted line) resulting from the natural linewidth (dashed line), the Doppler and Zeeman effects.

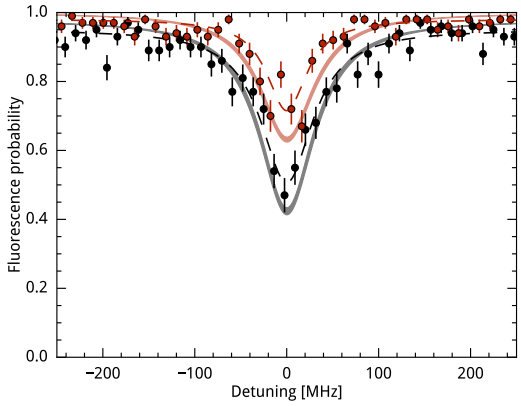


**Figure 10.** Comparison between the photon-recoil spectra of the $3s\ ^2\mathrm{S}_{1/2} \Leftrightarrow 3p\ ^2\mathrm{P}_{3/2}$ transition in $^{24}\mathrm{Mg}^+$ obtained using either one (red) or both (black) shelving pulses on $^{40}\mathrm{Ca}^+$ before readout. The lighter colored broader lines represent the simulated results when including the uncertainty (± one standard deviation) of the experimental value of $I_L$, while the dashed lines are Lorentzian fits to the experimental data. A ∼50 % increase in contrast is clearly seen. The spectroscopy laser light intensity is $I_L = 10(7)\,\mu\mathrm{W\,cm}^{-2} = 1.3 \times 10^{-5} I^t_{sat}$ and $\tau_{\mathrm{spec}} = 1.6(1)$ ms ($\tau_{scaled} = 5.6$). Note that the intensity of the spectroscopic pulse was increased by a factor two compared to the spectra in Fig. 5 and 9, to not be limited by the faster heating rate of the in-phase mode.

$I_L = 10(7)\,\mu\mathrm{W\,cm}^{-2} \approx 1.3 \times 10^{-5} I^t_{sat}$ with a spectroscopy excitation time of $\tau_{spec} = 1.6(1)$ ms ($\tau_{scaled} = 5.6$). Note that the intensity of the spectroscopic pulse was increased by a factor two compared to the spectra in Fig. 9, in order not to be limited by the faster heating rate of the IP mode as compared to the OP mode. Both experimental spectra have been centered at a detuning of 0 MHz, while the wavelength meter readings gave off-sets of 16(3) MHz and 20(3) MHz, respectively. These discrepancies are once again both within the inaccuracy of the wavelength meter.

### *3.2. Simulation of unresolved PRS due to laser linewidth*

In this section we present simulation results of mid-infrared vibrational PRS of the very narrow $|v = 0, J = 1\rangle$ - $|v' = 1, J' = 0\rangle$ transition ($\Gamma_t/2\pi = 2.50$ Hz) at 6.17 µm in the $^1\Sigma^+$ electronic ground state of $^{24}\mathrm{MgH}^+$ (See Fig. 11) by laser sources with varying linewidths from $\Gamma_L \sim 2\pi \times 10\,\mathrm{MHz}$ to 100 MHz. As for the $^{24}\mathrm{Mg}^+$ ion, the considered internal state structure does not really constitute a two-level system but a four-level one as shown in Fig. 11c. However, choosing for example a linearly polarized light source, absorption can only happen from a single rotational sub-state, the $m_J = 0$ state. Similarly, stimulated emission can only happen back to the same sub-state and an effective two-level scheme is established with respect to interactions with the light field. However, as in the case of the $^{24}\mathrm{Mg}^+$ ion, the saturation intensity has to be scaled by the norm squared of the relevant Clebsch-Gordan coefficient. This is implemented by dividing $R^{\mathrm{res,L}}_{\mathrm{abs},0}$ by 3 for both absorption and stimulated emission. The present level scheme has the further complication that population in the $m_J = \pm 1$ sub-states does not interact with the light field. Hence, if the molecular ion was originally in one of these sub-states (or if one of these sub-states were populated through spontaneous emission), it would not contribute (anymore) to the PRS signal. To avoid this effect, one can apply a magnetic field not aligned with the polarization axis of the light source, which would lead to Larmor precession of populations between the three sub-states of the $|v = 0, J = 1\rangle$ level. The situation becomes particularly simple when the

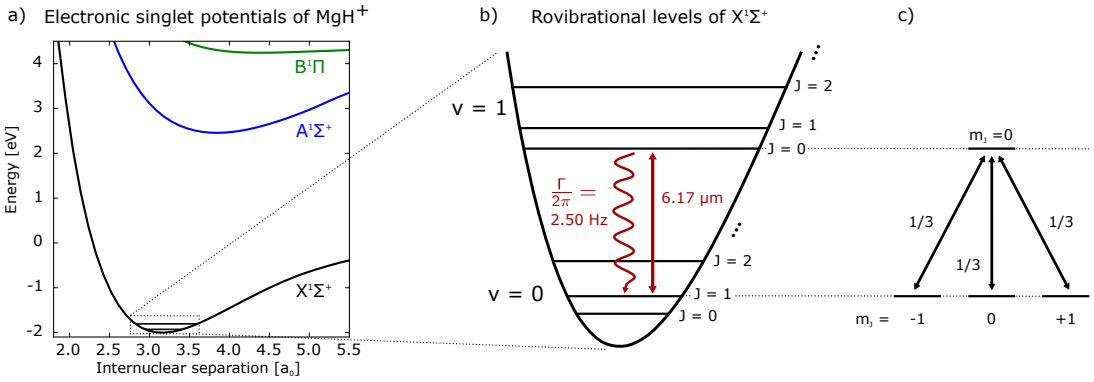


**Figure 11.** The electronic singlet potentials of $MgH^+$. Only the electronic ground state $X^1\Sigma^+$ is considered in the simulation. b) Rovibrational structure of the electronic ground state $X^1\Sigma^+$ showing the closed transition of interest $|v=0, J=1\rangle - |v'=1, J'=0\rangle$. The decay rate of $\Gamma_t = 2\pi \times 2.50$ Hz is the slowest timescale of our experiment and spontaneous emission is negligible. c) Sub-levels of the $|v=0, J=1\rangle$ and $|v'=1, J'=0\rangle$ states showing the norm square of the Clebsch-Gordan coefficients.

larmor frequency $\omega_{Larmor} \gg R_{abs}$. In this case, one can assume the total lower state population at any instance to be equally distributed between the three $m_J = 0, \pm 1$ sub-states, i.e. one third in each. Therefore we can re-establish an effective two-level scenario, but with the absorption rate (and not the stimulated emission rate) divided by another factor of 3. This leads to a saturation intensity 9 times larger than the one presented in Eq. (35). In the following simulations, we assume this picture to be true and also disregard the hyperfine splitting of the involved rotational levels. Indeed, the splitting is typically $\sim 10\,\text{kHz}$, which is much smaller than the linewidth of the light source. All hyperfine components are thus addressed and are hence of no importance for the PRS signal.

### *3.2.1. Absorption and stimulated emission*

We assume again $\omega_z = 2\pi \times 147.9\,\text{kHz}$ for a single $^{40}Ca^+$ ion, which leads to $\omega_{ip} = 2\pi \times 162.0\,\text{kHz}$ and $\omega_{op} = 2\pi \times 295.7\,\text{kHz}$ (only slightly different than for $^{24}Mg^+$). Both mode angular frequencies are at least about two orders of magnitude smaller than $\Gamma_L$. We are thus clearly in the regime where we can apply Eqs. (25)-(26) with Eq. (33). With $\lambda_t = 6.17\,\mu\text{m}$ for the target ion and the above mode angular frequencies, the LDPs are $\eta_{ip,t} = 0.0192$ and $\eta_{op,t} = 0.0224$ for the spectroscopy laser beam propagating along the $z$-axis. In the simulations to be presented below, we use, as in the case of $^{24}Mg^+$, the values $\eta_{ip,t} = 0.0136$ and $\eta_{op,t} = 0.0159$ in order to eventually compare these results with experiments that we are currently setting up. Here, the laser beam makes a 45° angle with the $z$-axis, and hence the LDPs are reduced by a factor $\sqrt{2}$. For the same reasons as stated in Sec. 3.1, the simulation results presented here should still be very representative of the expected experimental signals.

### *3.2.2. Spontaneous emission*

To simulate the effect of spontaneously emitted photons, according to Eq. (38) we have to take into account the particular emission pattern of the $|\nu=0, J=1\rangle \leftrightarrow |\nu'=1, J'=0\rangle$ transition (See Fig. 11). From this upper sub-level the spontaneous emission pattern is completely isotropic (i.e. angle independent), since it can decay to

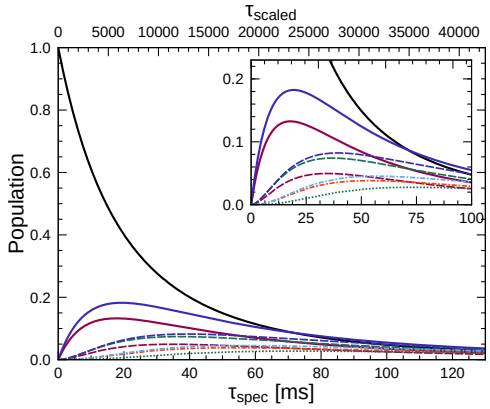


**Figure 12.** Simulated evolution of the population in different motional states as a function of spectroscopy time $\tau_{\rm spec}$ (bottom axis) and scaled time $\tau_{\rm scaled}$ (top axis) on resonance. The spectroscopy laser FWHM is $\Gamma_L = 2\pi \times 50$ MHz and intensity $I_L = 7.07\,{\rm W\,cm^{-2}} = 2.08 \times 10^4 I^L_{\rm sat}$. The following notation refers to motional states $(n_{ip}, n_{op})$: (0,0) ━━, (0,1) ━━, (1,0) ━━, (0,2) ╍╍, (1,1) ╍╍, (2,0) ╍╍, (1,2) ┅┅, (2,1) ┅┅, (2,2) ┈┈.

all lower sub-levels. The general form is thus:

$$W(\theta, \phi) = \frac{1}{4\pi}. \tag{43}$$

### *3.2.3. Basis for the numerical simulation*

The basis for the simulations is essentially the same as in Sec. 3.1.3. However, based on Eq. (20), which represents the relative coupling strengths of the various sidebands, we have found that, in this case, it suffices to take into account sidebands up to $s_{ip,max} = \pm 3$ and $s_{op,max} = \pm 3$. Because the mass ratios of the $^{40}Ca^+$ - $^{24}Mg^+$ and $^{40}Ca^+$ - $^{24}MgH^+$ systems are almost the same, we do not expect the mode coupling and thereby the heating rates from imperfect trapping conditions to be significantly different [19]. We thus use the same values of $R_{H,ip} = 14(1)\,{\rm s^{-1}}$ and $R_{H,op} = 1.7(3)\,{\rm s^{-1}}$, when modeling the $^{40}Ca^+$ - $^{24}MgH^+$ system.

### *3.2.4. Simulation of the dynamics of motional state populations on resonance*

In contrast to the simulations discussed in Sec. 3.1, here $\Gamma_L \gg \Gamma_t$ and according to Eq. (35) the saturation intensity $I^L_{sat}$ depends on the laser linewidth. As for the $^{24}Mg^+$ case, for laser intensities $I_L \ll I^L_{sat}$, we can ignore the stimulated emission terms in Eqs. (25-26), while in the case of $I_L \gg I^L_{sat}$, the spontaneous emission terms can be neglected. Since in the present case the spontaneous emission rate is similar to the trap heating rates, and the Lamb-Dicke parameters are much smaller than one, the trap heating influences the motional state dynamics much more strongly than spontaneous emission in all of the scenarios considered below.

Equivalently to the $^{24}Mg^+$ case we introduce the scaled time $\tau^L_{scaled} \equiv \tau_{spec} \times R^{{\rm res},L}_{{\rm abs},0}$. In Fig. 12, we show the evolution of the populations of the various motional states ($n_{ip}$, $n_{op}$) on resonance ($\omega_L = \omega_t$) as a function of real time $\tau_{spec}$ (bottom x-axis) and scaled time $\tau^L_{scaled}$ (top x-axis). Here, we take $\Gamma_L/2\pi = 50$ MHz and $I_L = 7.07$ Wcm$^{-2}$ $= 2.08 \times 10^4 I^L_{sat}$ with $I^L_{sat} = 3.40$ Wm$^{-2}$. As in Fig. 3, the motional ground state population (0,0) is a monotonically decreasing function of time. At short time the populations of all other motional states $(n_{ip}, n_{op}) \neq (0,0)$ increase linearly with

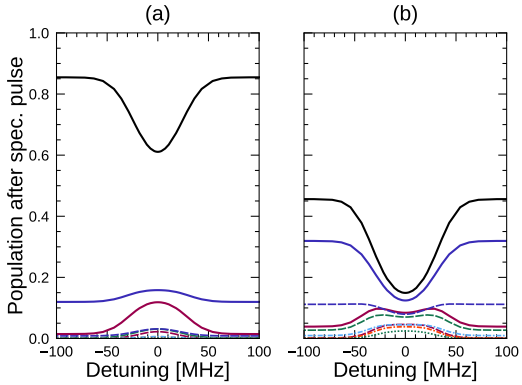


**Figure 13.** Simulated population in different motional states as a function of spectroscopy laser detuning, after spectroscopy times $\tau_{\mathrm{spec}}$ of 10 ms ($\tau_{\mathrm{scaled}} = 3280$) **(a)** and 50 ms ($\tau_{\mathrm{scaled}} = 16400$) **(b)**. The FWHM of the spectroscopy laser is $\Gamma_L = 2\pi \times 50$ MHz and the intensity is $I_L = 7.07\,\mathrm{W\,cm^{-2}} = 2.08 \times 10^4 I^L_{\mathrm{sat}}$. The following notation refers to motional states $(n_{ip}, n_{op})$: (0,0) ━━, (1,0) ━━, (2,0) ╍╍, (0,1) ━━, (1,1) ╍╍, (2,1) ┅┅, (0,2) ╍╍, (1,2) ┅┅, (2,2) ┅┅.

time, while for longer times, the rate of increasing population saturates and eventually decreases as a broader range of motional states is reached. The main reason for the difference in the dynamics of the excited motional state populations at a given scaled time, as compared to the $^{24}Mg^+$ case, is the different importance of trap heating.

### *3.2.5. Simulation of motional population spectra*

Scanning the laser frequency $\omega_L$ across the resonance of the $|v = 0, J = 1\rangle$ - $|v' = 1, J' = 0\rangle$ transition, we get the motional population spectra. In Fig. 13, we present two such spectra for $\Gamma_L/2\pi = 50$ MHz, $I_L = 7.07$ Wcm$^{-2}$ $= 2.08 \times 10^4 I^L_{sat}$ and for spectroscopy times $\tau_{spec} = 10$ ms and 50 ms ($\tau_{scaled} = 3280$ and 16400). For these parameters one clearly sees the effect of motional state depletion, but the higher weakly populated states now have a spectral response reflecting the gaussian linewidth of the laser. Another difference from the $^{24}Mg^+$ case is the increased background stemming from trap heating, effectively decreasing the signal depth. As evident from the solid and dashed blue curves, the much higher heating rate of the IP mode results in a much smaller signal depth. This clearly shows the advantage of performing readout on the OP mode instead of the IP mode.

### *3.2.6. Simulation of readout spectra*

To simulate the PRS spectrum, we follow the same recipe as in Sec. 3.1.6. In Fig. 14, we show readout spectra corresponding to the two population spectra in Fig. 13 after first having applied the readout pulse. The latter corresponds to a $\pi$-pulse with respect to the (0,1) $\rightarrow$ (0,0) 1st RSB of the $^{40}Ca^+$ quadrupole transition. With a transition wavelength of 729 nm, and the mode frequencies given above, we get $\eta_{ip,r} = 0.203$ and $\eta_{op,r} = 0.0949$. As for the $^{24}Mg^+$ case the fluorescence spectrum in Fig. 14b shows no sign of the depletion around resonance that could be seen in the corresponding population spectra presented in Fig 13b.

It is clear from Fig. 14 that there is a spectral broadening and an increase in signal depth with $\tau_{spec}$ for a fixed $R^{\mathrm{res},L}_{\mathrm{abs},0}$. However, the spectroscopic signal does not significantly change as long as $\tau_{\mathrm{scaled}}$ is a constant. This can be seen in Fig. 15 showing the signal FWHM and depth as a function of $\tau^L_{\mathrm{scaled}}$ for various laser intensities and

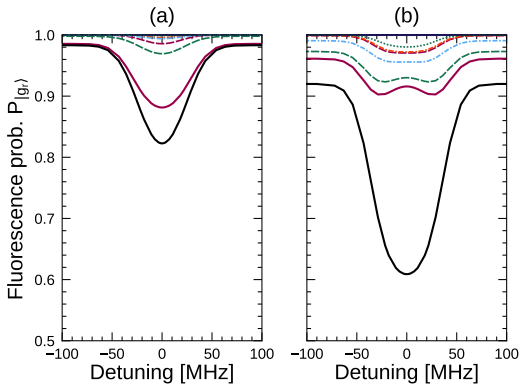


**Figure 14.** Simulated fluorescence probability $P_{|g_r\rangle}$, ▬, corresponding to the detected signal, for spectroscopy pulse lengths $\tau_{\rm spec}$ of 10 ms ($\tau_{\rm scaled} = 3280$) **(a)** and 50 ms ($\tau_{\rm scaled} = 16400$) **(b)** as a function of spectroscopy laser FWHM of $\Gamma_L = 2\pi \times 50$ MHz and intensity of $I_L = 7.07\,{\rm W\,cm^{-2}} = 2.08 \times 10^4 I^L_{\rm sat}$ on resonance. The remaining curves are the contributions from different motional states, corresponding to the terms in the sum of Eq. (40). The following notation refers to motional states $(n_{ip}, n_{op})$: (0,1) ▬, (1,1) ▬, (2,1) ▬, (0,2) ▬, (1,2) ▬, (2,2) ▬.

linewidths $\Gamma_L$. Here, the FWHM and signal depths have been found from graphical fits to the readout spectra, since the peak shapes deviate significantly from the Gaussian laser lineshape. The discrepancies between the different lines are due to trap heating. The FWHM at scaled times $\tau^L_{\rm scaled} \to 0$ has the expected value of the laser linewidth, and then increases almost linearly with $\tau^L_{\rm scaled}$.

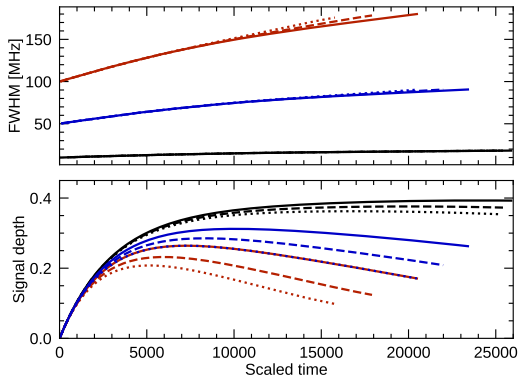


**Figure 15.** Numerically determined FWHM (top) and signal depth (bottom) of simulated fluorescence probability spectra as a function of scaled time for 3 different spectroscopy laser FWHM $\Gamma_L/2\pi$ of 10 MHz (▬), 50 MHz (▬), and 100 MHz (▬) and 3 different intensities: $I_L = 7.07\,{\rm W\,cm^{-2}}$ (solid), $I_L = 4.72\,{\rm W\,cm^{-2}}$ (dashed), $I_L = 3.54\,{\rm W\,cm^{-2}}$ (dotted). The deviation in signal depth for the different intensities is caused by heating from noise, which influences low intensities and broad spectroscopy laser linewidths more due to slower spectroscopy laser heating.

## 4. Discussion

In Sec. 3, we discussed in detail a model to describe the expected spectroscopic signals when applying photon recoil spectroscopy (PRS) in the unresolved sideband limit, where the frequency width of either the addressed transitions or the exciting light source are broader than the frequencies of the involved motional modes. As should be

evident from the simulation and experimental results, this particular scenario of PRS gives rise to some very particular features. One of them is a broadening of the spectroscopic signals that can be much larger than the natural linewidth of the transition or the spectral width of the applied light source. This broadening is highly dependent on the duration of the spectroscopic light pulse and exists even in cases where the interrogation intensities are far below the relevant saturation intensity (e.g. for the case of a broad transition discussed in sub-section 3.1).

At a first glance this situation may seem very unfortunate and disadvantageous with respect to applying unresolved PRS for any scientific investigations. However, in situations where the aim is to localize undetermined spectroscopic lines, this technique together with rather imprecise theoretical predictions of the line positions can turn out to be a very powerful tool to search for the transitions. More precise determination of the transition frequency can be achieved eventually by shortening the spectroscopic time and/or the frequency width of the interrogation light pulses to home in on the specific spectral line. Clearly, in the end, the width of the spectroscopic signal will be limited either by the linewidth of the transition addressed or the intrinsic width of the light source. Having initially a narrow laser source available, actively frequency broadening it during a line search phase seems advantageous compared to just stepping the frequency of the narrow laser through a certain (large) frequency interval.

A second important feature of unresolved sideband PRS is that the spectroscopic signal does essentially not depend on which of the two states of the transition is occupied by the target ion when applying the spectroscopic light pulses. In particular, in relation to localizing a narrow transition with an associated slow spontaneous decay rate, not to have to initialize the target ion in the lowest lying state before applying the spectroscopic light source can speed up the time that is otherwise required to obtain a spectrum. Indeed, as in the case considered in sub-section 3.2, the main contribution to the spectral broadening of the intrinsically narrow line stems from broadening of the motional state distribution due to light stimulated processes, i.e., absorption and stimulated emission.

This bring us finally to a short presentation of how one can, in a simple physical picture, understand the spectroscopic signals obtained in Sec. 3. While the initial internal state of the target ion is essentially irrelevant, the initial motional state of the two-ion system is highly important, since the spectroscopic signal is in essence a measure of how much population is left in the motional ground state after the application of the spectroscopic light pulse[3]. From this, one can understand the strong spectral broadening of the spectroscopic signal from a simple three-level picture. In this picture, in addition to the two transition levels, one considers a third auxiliary level that is populated whenever absorption or emission leads to a change in motional state away from the ground state. While in our presented model absorption and emission processes can also bring back population from excited motional states to the ground state, the general broadening with time of the motional state distribution will only lead to smaller deviations from the simple three level model. Simulations based on this very reduced picture gives results in close agreement with the full simulations, and qualitatively explain the spectral signal broadening by the fact that the signal is actually related to the depletion of the motional ground state. Since simulating the expected spectroscopic signal by this three-level scheme is several orders of magnitude faster than the full model presented in this paper, it can be a very useful tool as a

[3]It is in fact the following red sideband shelving pulse on the readout ion that allows for measuring the motional ground state population.

rough guide to optimize experimental parameters.

## 5. Conclusion

In conclusion, we have developed a model that can describe the expected spectroscopic signals when applying photon recoil spectroscopy (PRS) in the unresolved sideband limit where the linewidth of either the addressed transitions or the exciting light sources is broader than the frequencies of the involved motional modes. To test the model, we have presented experimental results with respect to the former case by carrying out unresolved sideband PRS on the 3s $^2S_{1/2}$ - 3p $^2P_{3/2}$ electronic transition of a single $^{24}Mg^+$ ion. Since a very good agreement has been obtained between our experimental and simulation results, we strongly believe the model to be useful for other spectroscopic investigations. In particular, since the technique does not require initialization of the target ion in one specific state of the transition, it should be very suited to localize still vastly unknown narrow lines in various target ions, such as rovibrational transitions in molecular ions and (hyper-)fine structure transitions in highly charged ions.

## Acknowledgements

S. M. and K. F. acknowledge support from the European Commission through the Marie Curie Initial Training Network COMIQ (grant agreement no 607491) under FP7. C. S. acknowledges support from the European Commission through the Marie Curie Individual Fellowship COMAMOC (grant agreement no 795107) under Horizon 2020. M. D. acknowledges support from the European Commissions FET Open TEQ, the Villum Foundation, the Sapere Aude Initiative from the Independent Research Fund Denmark, the Danish National Laser Infrastructure, LASERLAB.DK, established by the Danish Ministry of Research and Education.

## References

[1] K. Mølhave and M. Drewsen, "Formation of translationally cold $MgH^+$ and $MgD^+$ molecules in an ion trap," *Phys. Rev. A*, vol. 62, p. 011401, Jun 2000.

[2] G. Poulsen, *Sideband Cooling of Atomic and Molecular Ions*. PhD thesis, Aarhus University, Denmark, 2011.

[3] Y. Wan, F. Gebert, F. Wolf, and P. O. Schmidt, "Efficient sympathetic motional-ground-state cooling of a molecular ion," *Phys. Rev. A*, vol. 91, p. 043425, Apr 2015.

[4] R. Rugango, J. E. Goeders, T. H. Dixon, J. M. Gray, N. B. Khanyile, G. Shu, R. J. Clark, and K. R. Brown, "Sympathetic cooling of molecular ion motion to the ground state," *New Journal of Physics*, vol. 17, p. 035009, mar 2015.

[5] F. Wolf, Y. Wan, J. C. Heip, F. Gebert, C. Shi, and P. O. Schmidt, "Non-destructive state detection for quantum logic spectroscopy of molecular ions," *Nature*, vol. 530, feb 2016.

[6] C. Chou, C. Kurz, D. B. Hume, P. N. Plessow, D. R. Leibrandt, and D. Liebfried, "Preparation and coherent manipulation of pure quantum states of a single molecular ion," *Nature*, vol. 545, may 2017.

[7] M. Sinhal, Z. Meir, K. Najafian, G. Hegi, and S. Willitsch, "Quantum-nondemolition state

detection and spectroscopy of single trapped molecules," *Science*, vol. 367, pp. 1213–1218, mar 2020.

[8] Y. Lin, D. R. Leibrandt, D. Leibfried, and C.-w. Chou, "Quantum entanglement between an atom and a molecule," *arXiv preprint arXiv:1912.05866*, 2019.

[9] C. W. Chou, A. L. Collopy, C. Kurz, Y. Lin, M. E. Harding, P. N. Plessow, T. Fortier, S. Diddams, D. Leibfried, and D. R. Leibrandt, "Frequency-comb spectroscopy on pure quantum states of a single molecular ion," *Science*, vol. 367, pp. 1458–1461, mar 2020.

[10] P. O. Schmidt, T. Rosenband, C. Langer, W. M. Itano, J. C. Bergquist, and D. J. Wineland, "Spectroscopy using quantum logic," *Science*, vol. 309, no. 5735, pp. 749–752, 2005.

[11] Y. Wan, F. Gebert, J. B. Wübbena, N. Scharnhorst, S. Amairi, I. D. Leroux, B. Hemmerling, N. Lörch, K. Hammerer, and P. O. Schmidt, "Precision spectroscopy by photon-recoil signal amplification," *Nature communications*, vol. 5, p. 3096, 2014.

[12] F. Gebert, Y. Wan, F. Wolf, C. N. Angstmann, J. C. Berengut, and P. O. Schmidt, "Precision isotope shift measurements in calcium ions using quantum logic detection schemes," *Phys. Rev. Lett.*, vol. 115, p. 053003, Jul 2015.

[13] T. Rosenband, D. Hume, P. Schmidt, C.-W. Chou, A. Brusch, L. Lorini, W. Oskay, R. E. Drullinger, T. M. Fortier, J. Stalnaker, *et al.*, "Frequency ratio of $Al^+$ and $Hg^+$ single-ion optical clocks; metrology at the 17th decimal place," *Science*, vol. 319, no. 5871, pp. 1808–1812, 2008.

[14] M. Herrmann, V. Batteiger, S. Knünz, G. Saathoff, T. Udem, and T. W. Hänsch, "Frequency metrology on single trapped ions in the weak binding limit: The 3s $^2S_{1/2}$ - 3p $^2P_{3/2}$ transition in $^{24}Mg^+$," *Physical Review Letters*, vol. 102, Jan 2009.

[15] V. Batteiger, S. Knünz, M. Herrmann, G. Saathoff, H. A. Schüssler, B. Bernhardt, T. Wilken, R. Holzwarth, T. W. Hänsch, and T. Udem, "Precision spectroscopy of the 3s-3p fine-structure doublet in $Mg^+$," *Phys. Rev. A*, vol. 80, p. 022503, Aug 2009.

[16] A. K. Hansen, *Cold Molecular Ions: Rotational State Preparation and Single Ion Reaction Experiments*. PhD thesis, Aarhus University, Denmark, 2012.

[17] F. Jensen. Department of Chemistry, Aarhus University. Personal communication.

[18] D. J. Wineland, J. C. Bergquist, J. J. Bollinger, R. E. Drullinger, and W. M. Itano in *Proceedings of the 6th Symposium on Frequency Standards and Metrology* (P. G. W. S. Singapore), ed.), pp. 361–368, 2002.

[19] G. Morigi and H. Walther, "Two-species coulomb chains for quantum information," *The European Physical Journal D-Atomic, Molecular, Optical and Plasma Physics*, vol. 13, no. 2, pp. 261–269, 2001.

[20] M. Drewsen, A. Mortensen, R. Martinussen, P. Staanum, and J. L. Sørensen, "Nondestructive identification of cold and extremely localized single molecular ions," *Phys. Rev. Lett.*, vol. 93, p. 243201, Dec 2004.

[21] D. J. Wineland, C. Monroe, W. M. Itano, D. Leibfried, B. E. King, and D. M. Meekhof, "Experimental issues in coherent quantum-state manipulation of trapped atomic ions," *Journal of Research of the National Institute of Standards and Technology*, vol. 103, no. 3, p. 259, 1998.

[22] D. Leibfried, R. Blatt, C. Monroe, and D. Wineland, "Quantum dynamics of single trapped ions," *Rev. Mod. Phys.*, vol. 75, pp. 281–324, Mar 2003.

[23] J. B. Wübbena, S. Amairi, O. Mandel, and P. O. Schmidt, "Sympathetic cooling of mixed-species two-ion crystals for precision spectroscopy," *Phys. Rev. A*, vol. 85, p. 043412, Apr 2012.

[24] W. Magnus, "On the exponential solution of differential equations for a linear operator," *Communications on Pure and Applied Mathematics*, vol. 7, no. 4, pp. 649–673, 1954.

[25] D. J. Wineland and W. M. Itano, "Laser cooling of atoms," *Phys. Rev. A*, vol. 20, pp. 1521–1540, Oct 1979.

[26] S. Stenholm, "The semiclassical theory of laser cooling," *Rev. Mod. Phys.*, vol. 58, pp. 699–739, Jul 1986.

[27] R. Höppner, E. Roldán, and G. J. de Valcárcel, "A semiclassical optics derivation of

einsteins rate equations," *American Journal of Physics*, vol. 80, no. 10, pp. 882–890, 2012.

[28] J. D. Jackson, *Classical Electrodynamics*. John Wiley and Sons Ltd., 1962.